An adaptive isogeometric shell element for the prediction of initiation and growth of multiple delaminations in curved composite structures

Computers and Structures 260 (2022) 106701

Contents lists available at ScienceDirect

Computers and Structures

journal homepage: www.elsevier.com/locate/compstruc

An adaptive isogeometric shell element for the prediction of initiation and growth of multiple delaminations in curved composite structures

Elias Börjesson [a], Joris J.C. Remmers [b], Martin Fagerström [a,*]

[a] Department of Industrial and Materials Science, Chalmers University of Technology, Gothenburg, Sweden
[b] Department of Mechanical Engineering, Eindhoven University of Technology, PO Box 513, 5600 MB Eindhoven, the Netherlands

ARTICLE INFO

Article history:
Received 18 May 2021
Accepted 14 October 2021

Keywords:
Isogeometric analysis
Delamination
Stress reconstruction
Adaptivity

ABSTRACT

In order to model prominent failure modes experienced by multi-layered composites, a fine through-thickness discretisation is needed. If the structure also has large in-plane dimensions, the computational cost of the model becomes large. In light of this, we propose an adaptive isogeometric continuum shell element for the analysis of multi-layered structures. The key is a flexible and efficient method for controlling the continuity of the out-of-plane approximation, such that fine detail is only applied in areas of the structure where it is required. We demonstrate how so-called knot insertion can be utilised to automatise an adaptive refinement of the shell model at arbitrary interfaces, thereby making it possible to model multiple initiation and growth of delaminations. Furthermore, we also demonstrate that the higher-order continuity of the spline-based approximations allows for an accurate recovery of transverse stresses on the element level, even for doubly-curved laminates under general load. With this stress recovery method, critical areas of the simulated structures can be identified, and new refinements (cracks) can be introduced accordingly. In a concluding numerical example of a cantilever beam with two initial cracks, we demonstrate that the results obtained with the adaptive isogeometric shell element show good correlation with experimental data.

1. Introduction

Multi-layered composite structures, such as thin-walled fibre-reinforced laminates, exhibit many types of complex failure modes. Most of the underlying non-linear damage mechanisms are driven by a multi-axial stress state. Thus, for an accurate component design against damage initiation, it is crucial to be able to predict the complete three-dimensional stress state in an efficient manner.

Accordingly, much research has been conducted on stress predictions in laminated composites. Classical shell or plate theory, which utilises first order shear deformation theories, do not include the level of discretisation required to accurately predict the full stress state. As such, many researcher have developed theories with higher order approximation of the through-thickness displacement field to resolve this issue. These higher order theories have shown to yield good stress predictions, see e.g. Carrera [1] for a review of so-called Zig-Zag theories, Reddy [2] for higher order theories in laminated composites, and Carrera et al. [3] for the unification of higher order theories.

Furthermore, to also allow the simulation-driven design of a damage-tolerant component, the numerical models used must be capable of accurately capturing the interplay between several progressive failure modes. For many applications, this interplay of modes is strongly affected by the amount of delamination, see e.g. [4] for crash applications, making efficient and accurate modelling of delamination growth a necessity.

In industry, however, requirements on accurate 3D stress predictions and delamination growth capabilities are often in competition with a high demand for short simulation times (to allow for many design iterations). Thus, industry models are often discretised with an equivalent single layer (ESL) of shell elements, with or without plane stress assumptions, that incorporate the layered structure through a layered integration scheme and that adopts simplified kinematical assumptions for the through-thickness deformation. Thereby, such models lack both the capability for an accurate stress prediction [5,6] and the capability to model growth of delaminations.

In situations where progressive failure must be accounted for, ESL models are simply insufficient. Instead, models with a layer-wise (LW) discretisation are often proposed. In such models, some or (more commonly) all of the individual composite layers are resolved by one or more *continuum* or *continuum shell* elements,

* Corresponding author.
E-mail address: martin.fagerstrom@chalmers.se (M. Fagerström).

https://doi.org/10.1016/j.compstruc.2021.106701
0045-7949/

e.g. [7–12], respectively. The fine through-thickness discretisation results in an accurate prediction of the complete stress state, and allows for the modelling delamination growth e.g. through (adaptive) introduction of cohesive elements [13,14] or through the Virtual Crack Closing Technique [15,16]. Unfortunately, LW models are computationally heavy and infeasible for industrial component analysis.

An approach that combines the advantages of ESL and LW models is to make the through-thickness kinematics adaptive. Several different, but related approaches have already been proposed, see for example [17–22] to name a few. The key idea is to initialise the model with only ESL based elements, and then to refine the model in the areas where large deformations and/or stresses are detected. In this way, the model can remain largely efficient by only using detailed LW discretisation where it is needed.

Further gain can be obtained by developing an adaptive shell model based on Isogeometric Analysis (IGA), primarily for two reasons. Firstly, as demonstrated by several authors, the higher order continuity of the spline functions associated with IGA produce good results when used in shell and continuum-shell formulations [23,24]. As shown by [22,25], although for planar laminates only, the higher-order continuity also allows for an accurate element-wise recovery of transverse stresses. Secondly, Hosseini et al. [24] demonstrated that the so-called knot-insertion technique provides a flexible and straightforward approach of controlling the discretisation level in the through-thickness direction in a continuum-shell. This was further extended for planar laminates in Adams et al. [22], by introducing an automatic refinement of the through-thickness kinematics during simulation, thereby creating a fully adaptive model for single delamination growth. This makes it possible to mimic both the ESL and LW modelling approaches within one single shell implementation.

In the current paper, we propose a shell modelling approach, similar to Adams et al. [22], but with the additional capabilities to *i)* accurately recover through-thickness stresses *for arbitrarily curved laminates* and *ii)* adaptively model the initiation and growth of *arbitrarily many delamination cracks*. As a result, the proposed element is more applicable to industrial composite structures with complex shapes, and where many delaminations may occur through the thickness.

The paper is outlined as follows. Section 2 presents the shell kinematics used for the formulation of the shell. Next, Section 3 includes the extended formulation of through-thickness discretisation on which the adaptive shell element is based. In Section 4 we then present relevant implementation details, followed by the details of the stress recovery method for arbitrary shaped geometries in Section 5. In Section 6, we show the capabilities of the element in two numerical examples, demonstrating both an accurate stress recovery procedure and the ability to replicate experimental results with two growing (and competing) delamination cracks. Finally, Section 7 ends with some concluding remarks of the findings made in this paper.

2. Shell kinematics

The underlying shell kinematics is based on the work of Hosseini et al. [24], whereby only an overview is given here. Consider the undeformed and deformed configurations of a continuum shell in Fig. 1, with reference mid-surfaces S_0 and S, respectively. Let the mid-surface of the shell be described using two local curve-linear coordinates θ_1 and θ_2, and let θ_3 be the unit coordinate in the thickness direction. With these coordinates, the position of a material point within the shell body in the undeformed configuration can be expressed as:

$$\mathbf{X}(\theta_1,\theta_2,\theta_3) = \mathbf{X}^0(\theta_1,\theta_2) + \theta_3 \frac{t}{2}\mathbf{D}(\theta_1,\theta_2), \quad -1 \leqslant \theta_3 \leqslant 1 \tag{1}$$

where $\mathbf{X}^0$ is a material point on the mid-surface, t is the thickness of the shell, and $\mathbf{D}$ is a thickness director normal to the midsurface.

The covariant triad for any point within the undeformed shell is obtained as the partial derivatives of Eq. (1), with respect to the curvilinear coordinates,

$$\begin{aligned} \mathbf{G}_\alpha &= \frac{\partial \mathbf{X}}{\partial \theta_\alpha} = \mathbf{E}_\alpha + \theta_3 \frac{t}{2}\mathbf{D}_{,\alpha} \quad \text{with} \quad \alpha = 1,2 \\ \mathbf{G}_3 &= \frac{t}{2}\mathbf{D}, \end{aligned} \tag{2}$$

where $\mathbf{E}_\alpha$ and $\mathbf{D}$ are a covariant triad defined on the mid-surface of the shell, as:

$$\begin{aligned} \mathbf{E}_\alpha &= \frac{\partial \mathbf{X}^0}{\partial \theta_\alpha} \quad \text{with} \quad \alpha = 1,2 \\ \mathbf{D} &= \frac{\mathbf{E}_1 \times \mathbf{E}_2}{||\mathbf{E}_1 \times \mathbf{E}_2||}, \end{aligned} \tag{3}$$

and where the comma subscript $\bullet_{,\alpha}$ denotes partial differentiation with respect to θ_α.

The position of a material point in the deformed configuration $\mathbf{x}(\theta_1,\theta_2,\theta_3)$ can be expressed in terms of the undeformed configuration $\mathbf{X}(\theta_1,\theta_2,\theta_3)$ and a displacement field $\mathbf{u}(\theta_1,\theta_2,\theta_3)$ as:

$$\mathbf{x}(\theta_1,\theta_2,\theta_3) = \mathbf{X}(\theta_1,\theta_2,\theta_3) + \mathbf{u}(\theta_1,\theta_2,\theta_3). \tag{4}$$

Using the above relation, the covariant triad in the deformed shell element, $\mathbf{g}_i$, can be expressed as:

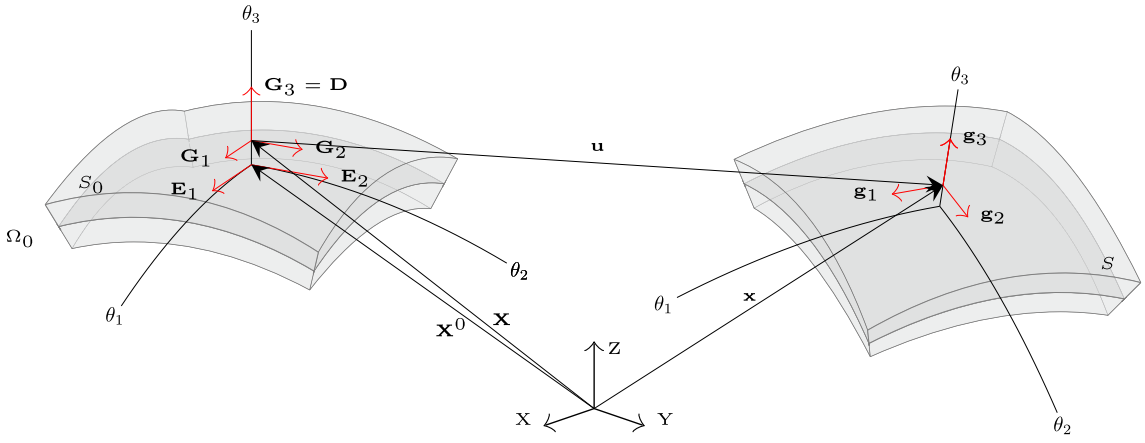

Fig. 1. Kinematics of the continuum shell in the undeformed and deformed configuration.

$$\mathbf{g}_i = \frac{\partial \mathbf{x}}{\partial \theta_i} = \mathbf{G}_i + \mathbf{u}_{,i} \quad \text{with} \quad i = 1,2,3. \tag{5}$$

The deformation gradient $\mathbf{F}$ is expressed as:

$$\mathbf{F} = \frac{\mathrm{d}\mathbf{x}}{\mathrm{d}\mathbf{X}} = \mathbf{g}_i \otimes \mathbf{G}^i, \tag{6}$$

where the contravariant basis $\mathbf{G}^i$ are related to the covariant basis via the metric tensor G^{ij}

$$\mathbf{G}^i = G^{ij}\mathbf{G}_j \qquad G_{ij} = \{G^{ij}\}^{-1} = \mathbf{G}_i \cdot \mathbf{G}_j. \tag{7}$$

For future use, the principal curvatures and their orientations on the surface S are needed. They can be determined from the Weingarten map [26]

$$\{\mathscr{W}_{\alpha\beta}\} = \{g_{\alpha\beta}\}^{-1}\{b_{\alpha\beta}\}, \tag{8}$$

defined in terms of the first ($g_{\alpha\beta}$) and second ($b_{\alpha\beta}$) fundamental form of the surface, obtained as

$$g_{\alpha\beta} = \mathbf{g}_\alpha \cdot \mathbf{g}_\beta, \quad b_{\alpha\beta} = \mathbf{g}_\alpha \cdot \mathbf{D}_{,\beta} \quad \text{with} \quad \alpha,\beta = 1,2. \tag{9}$$

The Weingarten map can be represented as a 2 by 2 matrix

$$\{\mathscr{W}_{\alpha\beta}\} = \begin{bmatrix} \kappa_{11} & \kappa_{12} \\ \kappa_{21} & \kappa_{22} \end{bmatrix}. \tag{10}$$

If the curve-linear coordinates θ_1 and θ_2 align with the principal curvature directions, the off diagonal terms κ_{12} and κ_{21} are zero, and the principal curvatures are directly determined by κ_{11} and κ_{22}. However, if these directions do not coincide, the principal curvatures and their directions can be obtained through an eigenvalue analysis of $\{\mathscr{W}_{\alpha\beta}\}$.

3. Spatial discretisation

For a smooth representation of the geometry and the displacement field, we adopt an isogeometric description. In this context, both the mid-surface and the displacement field is represented by spline functions. In particular, the displacement field introduced in Eq. (4) is discretised using a solid-shell discretisation,

$$\boldsymbol{u}(\theta_1,\theta_2,\theta_3) = \sum_{I=1}^{N_{\mathrm{cp}}} N_I(\theta_1,\theta_2,\theta_3)\boldsymbol{a}_I, \tag{11}$$

where N_I are trivariate spline functions, $\boldsymbol{a}_I$ is the vector containing the degrees of freedom at control point I, and $N_{\mathrm{cp}} = n \times m$ is the total number of control points, with n and m being the number of control points in the in-plane and out-of-plane directions, respectively. These functions are constructed as a combination of bivariate in-plane spline functions $S_i(\theta_1,\theta_2)$, and univariate out-of-plane B-Spline functions, $H_j(\theta_3)$ as:

$$\begin{aligned} N_I &= S_i(\theta_1,\theta_2)H_j(\theta_3) \\ I &= i + (j-1)n \\ i &\in [1,\dots n] \\ j &\in [1,\dots m] \end{aligned} \tag{12}$$

The in-plane functions $S(\theta_1,\theta_2)$ can be of the family of spline interpolation functions, such as B-Splines, NURBS, T-Splines, etc. In this paper we adopt NURBS [27], as it is widely supported by CAD software and modern mesh generators. The univariate B-spline functions $H_j(\theta_3)$ are defined by a knot vector Ξ, containing knot values ξ_i which represents coordinates in the parameter domain,

$$\Xi = \left[\xi_1, \xi_2, \dots, \xi_{l+p+1}\right], \tag{13}$$

where l is the number of spline functions, and p is the degree of the functions. The advantage of the split between the out-of-plane and in-plane basis functions is that the kinematics through the thickness of the shell can be modified in a flexible manner by inserting knots in the knot vector Ξ. By introducing multiple knots and thereby reducing the continuity in the thickness direction down to C^0, strain discontinuities occurring at material interfaces can be well represented. Furthermore, increasing the multiplicity yet one more time will introduce C^{-1} discontinuities, i.e. displacement discontinuities, whereby delamination cracks can be described.

Following Adams et al. [22], we consider three basic discretisation states for the control points in the through-thickness direction ($H_j(\theta_3)$): *lumped*, *layered* and *discontinuous*. Furthermore, we extend the method proposed therein by allowing for multiple delaminations at arbitrary interfaces in the shell. In order to describe the three states in more detail, consider a shell with three layers and a second order ($p = 2$) (out-of-plane) B-Spline representation, see Fig. 2.

- **Lumped**
  Control points in a *lumped* state, model the through-thickness section of a shell as a single element through the thickness. Thus this element is equivalent to an equivalent-single-layer model. As such, elements with *lumped* control points can predict the in-plane and bending stiffness as well as the in-plane stress state in an efficient manner, but lacks the capability to accurately predict the out-of-plane stresses in the shell [25]. For the case of having a quadratic B-spline interpolation H_j, see Fig. 2a, the knot vector will be $\Xi = [-1,-1,-1,+1,+1,+1]$.
- **Layered**
  By inserting multiple co-located knots in the knot vector (up to order of multiplicity p) at positions corresponding to the ply interface locations, i.e. such that $\Xi = \left[-1,-1,-1,-\frac{1}{3},-\frac{1}{3},+\frac{1}{3},+\frac{1}{3},+1,+1,+1\right]$, a *layered* representation can be constructed. This is equivalent to a so called layer-wise model, for which a C^0 discretisation is obtained through the thickness. As the kinematics are now refined through the thickness, to appropriately represent the strain-discontinuities observed in laminated composites, an element with control points in this state is able to accurately predict also the through-thickness stresses.
- **Discontinuous**
  By increasing the knot multiplicity equal to $p+1$, the B-splines can model discontinuities between the ply interfaces. Furthermore, by simultaneously introducing a cohesive interface

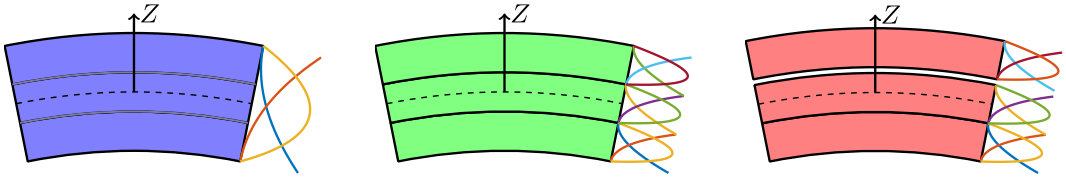

(a) *lumped* state (b) *layered* state (c) *discontinuous* state

Fig. 2. The three configurations considered in this work, denoted *lumped*, *layered* and *discontinuous*. The knot vectors, Ξ, are, a) $[-1,-1,-1,+1,+1,+1]$ b) $\left[-1,-1,-1,-\frac{1}{3},-\frac{1}{3},+\frac{1}{3},+\frac{1}{3},+1,+1,+1\right]$ and c) $\left[-1,-1,-1,-\frac{1}{3},-\frac{1}{3},+\frac{1}{3},+\frac{1}{3},+\frac{1}{3},+1,+1,+1\right]$.

relation at this discontinuity, the configuration is capable of representing initiating and/or propagating delamination cracks. For our example in Fig. 2c, a final knot has been inserted at $\frac{1}{3}$, resulting in the knot vector $\Xi = [-1,-1,-1,-\frac{1}{3},-\frac{1}{3},+\frac{1}{3},+\frac{1}{3},+\frac{1}{3},+1,+1,+1]$, allowing the top interface to separate.

In addition to the control point states described above, we also introduce the notion of element states. For example, if all the control points in an element are of the *layered* state, then the element state is also considered to be *layered*. Note, however, that an element can be supported by a mixture of the control points states presented above. This is a result from the fact that the control points in Isogeometric elements have support over multiple elements (depending on the degree of the shape-functions). In such cases, we denote the element state as *mixed*. One effect that extended control point support brings is that displacement discontinuities in *discontinuous* elements are extended into these *mixed* elements as well. Interested readers are referred to [22] for a more in-depth discussion on how this state can be handled in the numerical implementation.

4. Adaptive refinement to represent multiple delaminations

In the previous section we showed how the proposed discretisation of the kinematical states can be used to represent multiple delaminations. In the following sections, we discuss relevant issues that arise when implementing such a formulation into an adaptive simulation scheme. We start by suggesting a method for when to refine the element state in critical areas. Next, we also explain how the new degrees of freedom that are introduced in a refinement step are initialised correctly.

4.1. Refinement criterion

For a modelling approach that adaptively represents delamination, it is important to ensure that, *i)* new delaminations can form in previously undamaged areas and *ii)* already existing cracks are able to propagate. In the sections below, we propose separate methods that address these points.

4.1.1. Initiation criterion

In order to determine when to initiate new delamination zones (by refining the kinematics and inserting cohesive elements), a criterion based on the stress state of the shell is used. We choose to adapt a quadratic failure criterion proposed by Ochoa and Engblom [28]. It is based on the tensile transverse normal and the shear stress resultant:

$$f_{\mathrm{I}} = \frac{\langle \sigma_{33} \rangle_+^2}{\sigma_{\mathrm{fn}}^2} + \frac{\sigma_{13}^2 + \sigma_{23}^2}{\sigma_{\mathrm{fs}}^2} \geqslant r_{\mathrm{I}}^2, \quad 0 < r_{\mathrm{I}} < 1 \tag{14}$$

where $\langle \bullet \rangle_+$ denotes the positive Macaulay brackets, and where σ_{fn} and σ_{fs} are, respectively, the interlaminar normal (tensile) and shear strength. The criterion is fulfilled when it reaches a certain threshold, specified by the parameter r_{I}. We recommend to set r_{I} to be less than one, otherwise the newly inserted cohesive zone might enter a damaged state immediately, which can lead to convergence issues.

Remark. It is important to note that the accuracy of the predicted transverse stress components will depend on the kinematical state of the shell element. If the element state is in a *layered* state, this kinematical representation yields sufficiently accurate stress predictions to be used in the failure criterion. On the other hand, if the element is in a *lumped* state, the transverse stresses computed from the element kinematics and the constitutive relation are in general not very accurate. As a remedy, we propose to adopt a stress recovery technique to compute these transverse stress components with a much higher accuracy, similarly to Främby et al. [21]. Further details of this recovery technique is given in Section 5, where we also show that this recovery can be made efficiently on a single element level, and provides accurate results for doubly curved surfaces under general loads.

4.1.2. Expansion criterion

In order to correctly model the propagation of delaminations, it is important that the cohesive zone is large enough to properly capture the kinematics and traction profile in front of the crack. We can ensure this by enforcing that a number of control points in the neighbourhood of the crack tip are in a *discontinuous* state. This also allows the delamination to propagate uninterruptedly, and to not get stuck in areas that are unable to represent separation between the interfaces (i.e areas with *lumped* or *layered* control point states).

We choose to adopt an expansion criterion proposed by Främby et al. [21], which is based on the damage variable of the cohesive zones. After each converged time step, the damage variable in all cohesive elements are checked to see if they exceeds a threshold parameter. The criterion can be formulated in a simple equation,

$$f_{\mathrm{p}} = 1 \quad \text{if} \quad d > r_{\mathrm{p}} \tag{15}$$

where f_{p} is the damage criterion, d is the damage variable of the cohesive zone model, and r_{p} is the threshold parameter. When the damage variable for a quadrature point within a cohesive zone element fulfills the above requirement, a radial search around the current element's control points is performed. Control points that are within this search radius, and which are not currently representing interface separation (i.e are in a *lumped* or *layered* state), are then added to the enrichment process. The size of the search radius, in which new control points should be included, is an input parameter for the simulation. Appropriate values for the radius can be determined from the cohesive zone length, which in turn can be estimated based on the cohesive material properties, see for example Turon et al. [29].

4.2. Initialisation of new degrees of freedom

Through-thickness kinematic refinement is performed by inserting new knots at the interface locations of the knot vector, as explained in Section 3. This step introduces additional degrees of freedom through the thickness of the shell, which need to be initialised. It is also important to note that due to the non-interpolatory nature of B-Splines, already existing degrees-of-freedom might need to be recomputed.

The initialisation (and re-initilisation) of degrees of freedom, can be performed by using a technique similar to the Beziér extraction technique used in Isogeometric Analysis [30]. The new degrees of freedom, $\mathbf{a}_{\mathrm{new}}$ (i.e. the displacements for the out of plane control points), are computed by,

$$\mathbf{a}^i_{\mathrm{new}} = \mathbf{C}\mathbf{a}^i_{\mathrm{old}}, \tag{16}$$

where $\mathbf{C}$ is the Beziér extraction matrix, $\mathbf{a}_{\mathrm{old}}$ is the degrees of freedom before the refinement, and i denotes a planar control points. This procedure is exemplified in the Fig. 3, where a shell with three layers and with control points in a *lumped* configuration, is enhanced to state where to top interface is *discontinuous*.

5. Recovery of transverse stress components

To keep the computational cost for the structural model as low as possible, all elements (except for regions where there might be pre-existing delaminations or obvious stress concentrations)

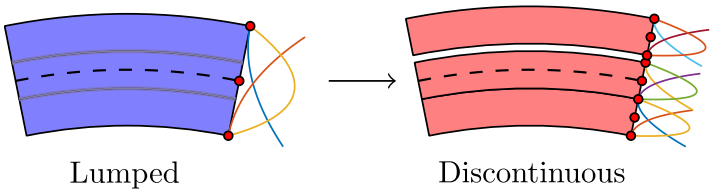

$$\mathbf{C}^T = \begin{bmatrix} 1 & \frac{6}{9} & \frac{4}{9} & \frac{2}{9} & \frac{1}{9} & \frac{1}{9} & 0 & 0 \\ 0 & \frac{3}{9} & \frac{4}{9} & \frac{5}{9} & \frac{4}{9} & \frac{4}{9} & \frac{3}{9} & 0 \\ 0 & 0 & \frac{1}{9} & \frac{2}{9} & \frac{4}{9} & \frac{4}{9} & \frac{6}{9} & 1 \end{bmatrix}$$

Fig. 3. The Beziér extraction operator, $\boldsymbol{C}$, used for determining new values of degrees of freedom, when an control point is enhanced from *Lumped* to *Discontinuous* state (with one interface crack).

should initially be in a lumped state. However, due to the low order discretisation of the out-of-plane strain components in the *lumped* element formulation, the transverse stresses may then be poorly predicted. The in-plane stresses on the other hand, are nonetheless accurately predicted by the *lumped* shell. Therefore, a method which improves the transverse stress prediction is needed.

One approach which has proven to be effective in this regard, is the so-called stress recovery approach, see for example Daniel et al. [6] or Dufour et al. [25]. The key point of this method is to recover the out-of-plane stresses using the momentum balance equations. Thereby, more accurate values of the transverse stress components can be obtained via numerical integration of the in-plane-stresses and their first and second derivatives.

In this context, IGA brings a significant advantage over the traditional finite element method, namely the fact that the spline functions used for the IGA discretisation are higher-order continuous over element boundaries. This results in a smooth stress field over the entire domain (or patch), which is in contrast to the discontinuous stress field at element boundaries generally obtained when using Lagrange polynomials as approximation functions in FE. The smoothness of the stress field obtained in IGA thereby allows for an accurate computation of first and second (depending on the IGA approximation) order derivatives of the stress field directly in a single point. This is highly beneficial as it allows the stress recovery to be conducted element-wise (in any specific location). In comparison, traditional FE generally first requires a non-local (element patch-wise) stress-smoothing operation before the stress derivatives can be estimated [21].

Many authors have successfully shown the effectiveness of the stress recovery technique for flat plates, where they base the method on the momentum balance (or equilibrium) equations considered in a Cartesian coordinate system. However, directly transferring this technique to more general shaped geometries, for example singly or doubly curved shapes, may lead to significant errors caused by the neglect of the geometric curvature. In order to get acceptable results for such geometries, the stress recovery method must either be *(i)* derived from the momentum balance (or equilibrium) equations expressed in a curve-linear coordinate system (see e.g. Daniel et al. [6]), or *(ii)* applied in a local Cartesian coordinate system, as recently demonstrated by Patton et al. [31]. In this work, we choose to investigate and develop the latter approach due to interesting advantages obtained by using an IGA-framework. The utilization of splines as a basis for the geometrical representation means that the curvature of the shell is well defined in the entire domain/patch. This is normally not the case in standard FE-elements, where often a piece-wise linear approximation of the geometry is assumed (even for higher order elements).

5.1. Stress recovery in curved shells

Consider a curve-linear coordinate system oriented according to the principal curvature directions (ξ_1, ξ_2, z), see Fig. 4 (note that the ξ_1 and ξ_2 does not necessarily align with the coordinates θ_1 and θ_2 introduced in Section 2). The equations governing the equilibrium of a stressed body (with body and inertia forces neglected) are given as [32],

$$\sum_{j=1}^{3}\left(\frac{h_1 h_2 h_3 h_i}{h_j}\sigma_{ij}\right)_{,j} - \sum_{j=1}^{3}\frac{h_1 h_2 h_3 h_{j,i}}{h_j}\sigma_{jj} = 0, \tag{17}$$

where σ_{ij} are the Cauchy stress components, h_i are functions of position in the curve-linear coordinate system, and $\bullet_{,i}$ denotes derivative with respect to ξ_i. In the framework for shells by Reddy [2], these can be expressed as

$$h_1 = a_1\lambda_1, \quad h_2 = a_2\lambda_2, \quad h_3 = 1. \tag{18}$$

Here, λ_i and the scale factors a_i are defined as:

$$\lambda_i = 1 + \kappa_i z \qquad a_\alpha = \sqrt{\bar{\mathbf{g}}_\alpha \cdot \bar{\mathbf{g}}_\alpha} \quad \text{with} \quad \alpha = 1, 2, \tag{19}$$

where κ_i are the principal curvatures κ_i, see Eq. (8).

In Eq. (19), $\bar{\mathbf{g}}_\alpha$ are the tangent vectors of the mid-surface in the direction of ξ_1 and ξ_2,

$$\bar{\mathbf{g}}_\alpha = \frac{\partial \mathbf{x}^0}{\partial \xi_i}, \tag{20}$$

where $\mathbf{x}^0$ is the mid-surface in the deformed configuration. The governing equation in Eq. (17) are integrated over the thickness of the shell in order to obtain expressions for the transverse stresses as [6]

$$\sigma_{13} = -\frac{1}{\lambda_1^2\lambda_2}\int_{-t/2}^{z}\left(\frac{\lambda_1\lambda_2}{a_1}\sigma_{11,1} + \frac{\lambda_1^2}{a_2}\sigma_{12,2} + \frac{\lambda_1^2 a_{2,1}}{a_1 a_2}(\sigma_{11} - \sigma_{22}) + \frac{2\lambda_1\lambda_2 a_{1,2}}{a_1 a_2}\sigma_{12}\right)dz + \frac{C_1}{\lambda_1^2\lambda_2}, \tag{21}$$

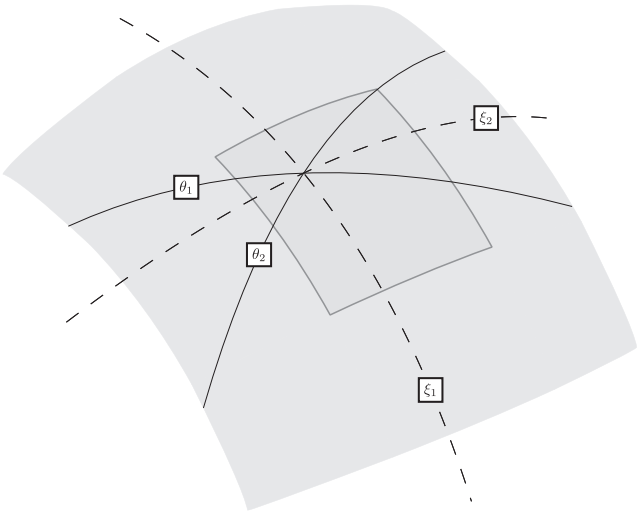

Fig. 4. A shell with two curve-linear coordinate systems. Note that the orthogonal curve-linear coordinates (ξ_1, ξ_2, z) are not necessarily aligned with the coordinates $(\theta_1, \theta_2, \theta_3)$ introduced in Section 2.

$$\sigma_{23} = -\frac{1}{\lambda_1\lambda_2^2}\int_{-t/2}^{z}\left(\frac{\lambda_1\lambda_2}{a_2}\sigma_{22,2}+\frac{\lambda_2^2}{a_1}\sigma_{12,1}+\frac{\lambda_2^2 a_{1,2}}{a_1 a_2}(\sigma_{22}-\sigma_{11})+\frac{2\lambda_1\lambda_2 a_{2,1}}{a_1 a_2}\sigma_{12}\right)dz + \frac{C_2}{\lambda_1\lambda_2^2}, \tag{22}$$

$$\sigma_{33} = -\frac{1}{\lambda_1\lambda_2}\int_{-t/2}^{z}\left(\frac{\lambda_2}{a_1}\sigma_{13,1}+\frac{\lambda_1}{a_2}\sigma_{23,2}-\kappa_1\lambda_2\sigma_{11}-\kappa_2\lambda_1\sigma_{22} + \frac{\lambda_1 a_{2,1}}{a_1 a_2}\sigma_{12}+\frac{\lambda_2 a_{1,2}}{a_1 a_2}\sigma_{23}\right)dz+\frac{C_3}{\lambda_1\lambda_2}, \tag{23}$$

where (again) t is the thickness of the laminate, and C_1, C_2 and C_3 are constants arising from the integration. These constants are determined from the traction conditions on the top and bottom surface.

Following the argumentation of Daniel et al. [6], we propose a modified version of the equation for σ_{33}. First, it is assumed that the derivatives of the transverse shear stresses can be omitted since they often have a negligible effect on the final stress values. Secondly, in order to fulfill the boundary conditions for σ_{33} on the top and bottom surfaces, an additional linear term is added to Eq. (24). With these two modifications, the simplified version of Eq. (24) becomes

$$\sigma_{33} = \frac{1}{\lambda_1\lambda_2}\int_{-t/2}^{z}\left(\kappa_1\lambda_2\sigma_{11}+\kappa_2\lambda_1\sigma_{22}-\frac{\lambda_1 a_{2,1}}{a_1 a_2}\sigma_{12}-\frac{\lambda_2 a_{1,2}}{a_1 a_2}\sigma_{23}\right)dz + \frac{C_3+zC_4}{\lambda_1\lambda_2}, \tag{24}$$

where C_4 is a constant accounting for the linear term.

In the remainder of this work, the coordinates θ_1 and θ_2 (introduced in Section 1 for describing the mid-surface of the geometry), are assumed to be aligned with ξ_1 and ξ_2 (principal curvature coordinates). This can be achieved through a careful construction of the geometrical representation of the mid-surface. A consequence of this is that no transformation is required between the two coordinate systems.

5.2. Derivatives of the stresses

There are multiple options for determining the spatial derivatives of the in-plane stresses in Eqs. (21) and (22). Firstly, one can obtain the stress gradients by differentiating the constitutive equations directly as

$$\boldsymbol{\sigma} = f(\boldsymbol{\varepsilon}) \quad \Rightarrow \quad \boldsymbol{\sigma}_{,\alpha} = \frac{\partial f(\boldsymbol{\varepsilon})}{\partial \xi_\alpha}, \tag{25}$$

where $f(\boldsymbol{\varepsilon})$ represents the constitutive relation and $\boldsymbol{\varepsilon}$ represents the strain. This approach has the benefit of returning the exact stress gradients. The drawback however, is that an expression for the analytical form of the derivatives has to be derived for each unique material model that is used. Although tools such as automatic differentiation could be used, we have instead decided for another strategy.

Since the stress tensor is computed and stored for each quadrature point during the integration of the internal forces, we propose to use this pre-computed information to find an approximation of the stress gradients. This can be achieved by fitting a Lagrange polynomial to the quadrature points, which in turn can be used to interpolate the stress values as

$$\boldsymbol{\sigma} = \sum_{I=1}^{n} M_I(\xi_1,\xi_2)\hat{\boldsymbol{\sigma}}_I, \tag{26}$$

where M_I are the Lagrange basis functions, $\hat{\boldsymbol{\sigma}}_I$ are the stresses at the quadrature points, and n are number of quadrature points (and Lagrange polynomials). The stress gradients can then be obtained by taking the derivative of the interpolation

$$\boldsymbol{\sigma}_{,\alpha} = \sum_{I=1}^{n} \frac{\partial M_I(\xi_1,\xi_2)}{\partial \xi_\alpha}\hat{\boldsymbol{\sigma}}_I. \tag{27}$$

In contrast to the first method, presented in Eq. (25), this second method is favourable as it directly applies to all constitutive models. Furthermore, it is computationally efficient since it uses already computed values. Also, although this method does not allow the exact computation of stress derivatives, the results shown in the numerical examples in Section 6 still indicate a good accuracy of the method.

6. Numerical examples

The capabilities of the adaptive isogeometric shell element are presented next. First we showcase the effectiveness and generality of the stress recovery method presented in Section 5. Then, the shell element is applied to a multi-layered structure, where multiple independent crack growth is present.

6.1. Prediction of transverse stresses in a doubly-curved shell

Inspired by Daniel et al. [6] we consider the doubly curved shell geometry as shown in Fig. 5. The radii of curvature at the mid-surface are $R_1 = 25$ mm and $R_2 = 10$ mm, respectively. The bottom edge of the surface is clamped, while a traction is applied on the upper edge[1]. Furthermore, the laminate considered for the shell has a quasi-isotropic, non-symmetric layup with fibre orientations $[0, 90, 45, -45]$, where each layer is 0.2 mm thick, and has material properties according to Table 1.

Two cases for the applied traction are considered. In the first case, a constant traction is applied in the Z-directions, $t_z = -\sigma_0$, resulting in a pure bending load and subsequent deformation. In the second case, a twisting mode is considered by applying a vertical traction that varies along the X-direction as $t_z(x) = \sigma_0 x$ (see the figure for the definition of the coordinate axes). This second load case will naturally introduce a twisting mode of deformation, for which transverse stresses cannot as easily be recovered well using classical approaches such as the extended 2D-method [5].

The recovered stresses are evaluated through the thickness in a point located at the center of both curvatures (see the red point in Fig. 5). For the first case, with a constant traction applied in the z-direction, a discretisation with 24×16 control points (21×13 elements) and third order in-plane approximation has been used. For the second case, with an applied twisting moment, it was found that a finer discretisation and a higher order approximation is required in order to obtain a converged solution. This is an effect from the interaction between the complex geometry and the twisting moment, leading to slowly converging stress gradients. As such, a finer discretisation together with higher order shape functions has been used; 25×31 control points (21×27 elements) and fourth order shape functions. For both cases, a second order B-spline approximation and two quadrature points in the out-of-plane directions have been used.

To verify the recovered stresses, results will be compared against a reference solution obtained using elements in a layered state. A high fidelity discretisation has been used, with 45×45 control points (41×41 elements) and fourth order shape functions. Note that the reference solution is integrated with standard Gauss integration, which is why the top and bottom values are not exactly at $z = \pm h/2$.

The results for both load cases ($t_z = -\sigma_0$ and $t_z = \sigma_0 x$) are presented in Figs. 6 and 7, respectively. In both cases, the recovered

[1] The example has been slightly modified in regards to how the load is applied, in order for easier implementation in non-commercial FE-codes.

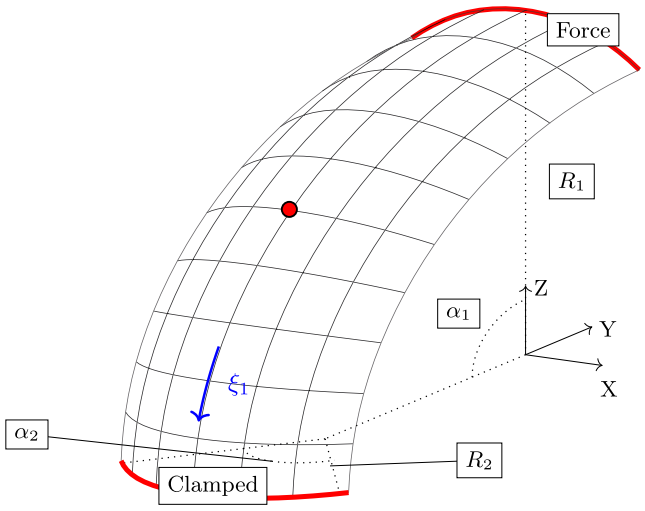

Fig. 5. The doubly-curved geometry considered for stress recovery. The geometrical properties are $R_1 = 25$ mm, $R_2 = 10$ mm, $\alpha_1 = 90°, \alpha_2 = 95°$.

Table 1
Material parameters used for the stress recovery example.

E_1	100 GPa	G_{12}	5 GPa	ν_{12}	0.25
E_2	10 GPa	G_{13}	5 GPa	ν_{13}	0.25
E_3	10 GPa	G_{23}	5 GPa	ν_{23}	0.25

stress components show good agreement with the reference solution. Furthermore, the stresses on the top and bottom surfaces show good agreement with the traction free boundary conditions. It can be concluded that the stress recovery greatly improves the prediction of the out-of-plane stress components, which therefore can be used for an accurate evaluation of the failure criterion Eq. (14).

6.2. Adaptive modelling of the growth of two delamination cracks

In the next example, we model a composite structure with two competing delaminations, in order to demonstrate the adaptive capabilities of the shell. For this purpose, we consider a multiple end-loaded-split specimen that previously has been analysed both experimentally and numerically by Yasaee et al. [33]. The load case has been designed such that unstable and independent crack propagation of two different cracks is obtained.

Fig. 8 shows the geometrical setup and boundary conditions for the problem. The length, width and thickness of the beam are $L = 115$ mm, $W = 20$ mm and $H = 8$ mm, respectively. Furthermore, two initial delamination cracks have been introduced at $z = 2$ mm and $z = 6$ mm, having initial lengths of 32 mm and 54 mm, respectively. Following Yasaee et al., the boundary at $x = 0$ mm is fixed in the Y- and Z-directions, while the top edge at $x = 115$ mm is constrained in the X-direction. Furthermore, at $x = 10$ mm, the bottom side is constrained in the Z-direction. This setup of the displacement boundary conditions is used to emulate the compliance obtained from the experimental testing. Finally, a force is applied on the top edge of at $x = 115$ mm.

The test specimen is made from an IM7/8552 unidirectional prepreg [34], stacked in a quasi-isotropic sequence of $(0/-45/90/45)_{2s}//\left[(0/-45/90/45)_{2s}\right]_2//(0/-45/90/45)_{2s}$ (64 layers in total), where each laminae has a thickness of 0.125 mm (note that the // indicate the layers where the initial cracks are located). Following Yasaee et al., the elastic in-plane behaviour of

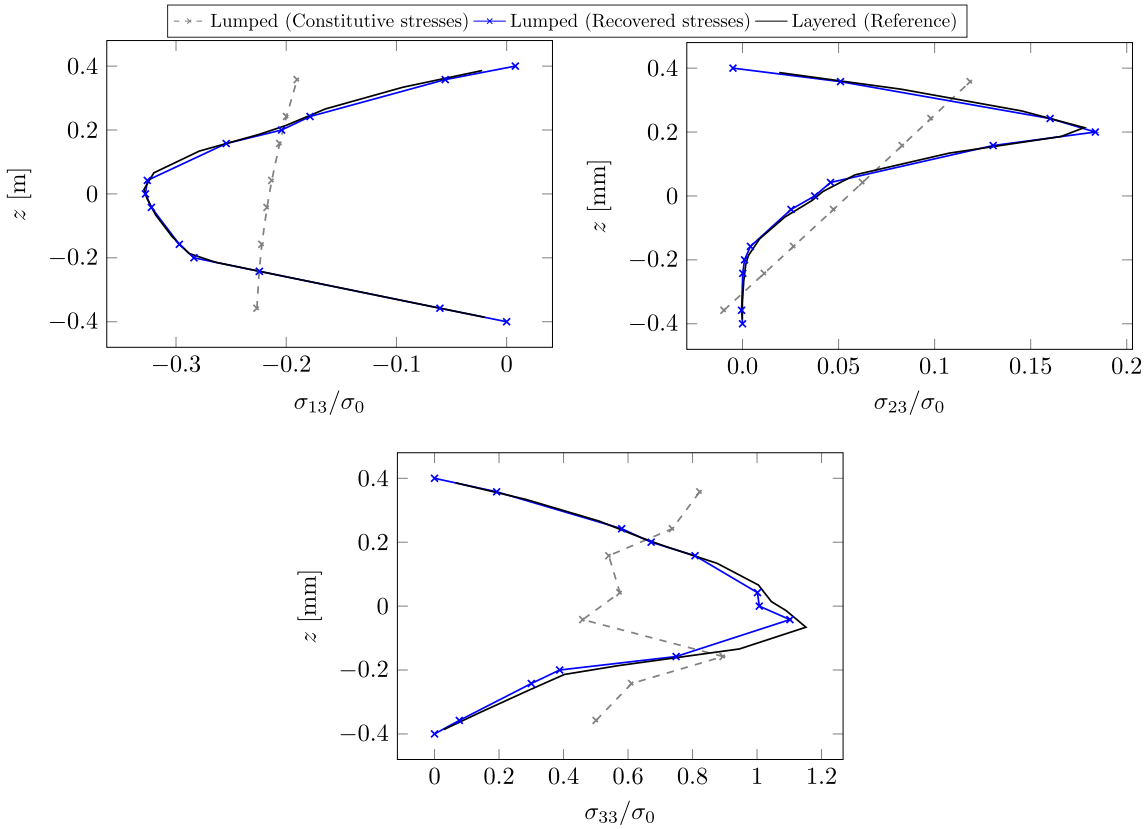

Fig. 6. Transverse stresses obtained at the mid-point of the doubly curved geometry, in the case of an applied force in the Z-direction.

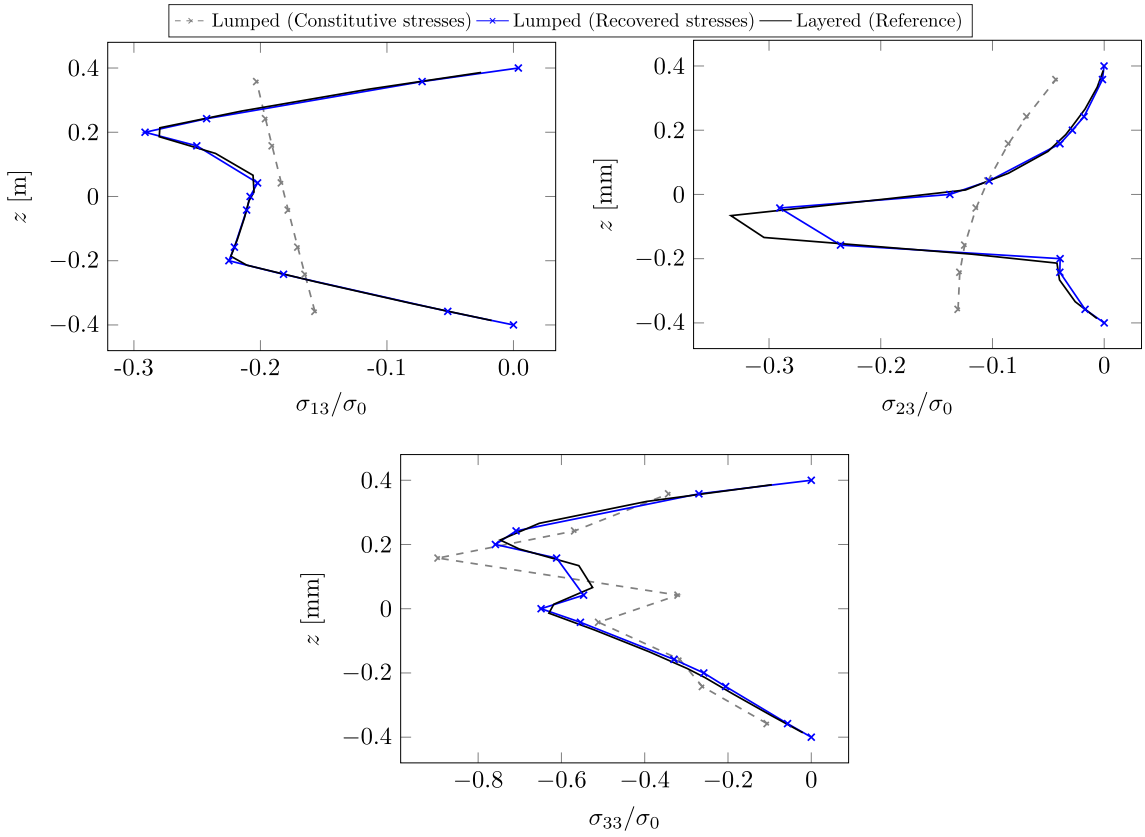

Fig. 7. Transverse stresses obtained at the mid-point of the doubly curved geometry, in the case of an applied twisting force.

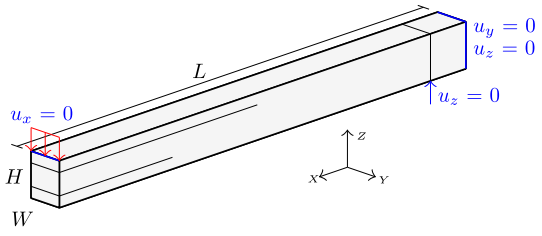

Fig. 8. The numerical example with multiple end-load-split.

the sublaminate stacking sequence $(0, -45, 90, 45)_{2s}$ has been homogenised into equivalent quasi-isotropic elastic properties, summarised in Table 2. This promotes efficiency and allows for only four equivalent (sublaminate) layers to be modelled.

Furthermore, in the specimens used for the experiments, a 13 μm thick PTFE release films were placed at the ply interfaces where the initial cracks are located. This was made in order to prevent any out-of-plane crack migration during growth. To simulate the degradation of these interfaces, an exponential cohesive law from [35] is used in this work. The fracture toughness in mode I and mode II are directly taken from [33] as G_{IC} = 211 J/m^2 and G_{IIC} = 1,050 J/m^2, respectively. In order to reduce the element size required to capture the traction profile in front of the crack tip, the ultimate tractions in mode I and mode II are halved compared to the values reported in the same paper, thus herein set to $\sigma_{I,max}$ = 30 MPa and $\sigma_{II,max}$ = 45 MPa, respectively. This assumption does not affect the results noticeably, since the crack propagation is mainly affected by the energy release rate of the cohesive zone.

Table 2
Effective in-plane properties (IM7/8552) (0/ −45/ 90/ 45).

E_1	61.65 GPa	G_{12}	23.37 GPa	ν_{12}	0.3187
E_2	61.65 GPa	G_{13}	4.55 GPa	ν_{13}	0.3161
E_3	13.61 GPa	G_{23}	4.55 GPa	ν_{23}	0.3161

The beam is herein modeled with second order B-splines in both in-plane and out-of-plane directions. In order to sufficiently resolve the cohesive zone, 117 control points (115 elements) are used along the beam. Furthermore, the results will be compared with an non-adaptive model, with pre-defined interface elements along the specimen. The adaptive model will initially have 8,235 degrees of freedom, as opposed to 11,403 degrees of freedom for the non-adaptive model.) The 10 left-most elements (close to the boundary condition) are fixed to the *layered* configuration. This is to accommodate for the compliance in the boundary condition in the experimental setup. The remaining elements are initialized either in a *lumped* configuration or a *discontinuous* configuration, the latter in a region where the initial cracks are present. For the refinement criteria presented in Section 4.1, we set $r_p = 0.01$ (r_I is not required in this example). Finally, since the crack growth is unstable and causes snap-back behaviour, the problem is solved using an arc-length solver with dissipation control [36].

The resulting force–displacement curve obtained with the adaptive isogeometric shell model is shown in Fig. 9, together with the corresponding curves from a non-adaptive shell model and from the experiments conducted by Yasaee et al. As can be observed, the resulting force–displacement curves from the adaptive and the non-adaptive simulations show good agreement with each other. Compared to the experimental curve, the adaptive and non-adaptive models predict the maximum peak loads accurately (4% error for first force drop, and 2% error for the second force drop).

In Fig. 10, the element configuration and the interface damage is shown for four different time instants through the adaptive analysis. At the first time step, the initial cracks are represented with discontinuous elements with a fully damaged interface. In subse-

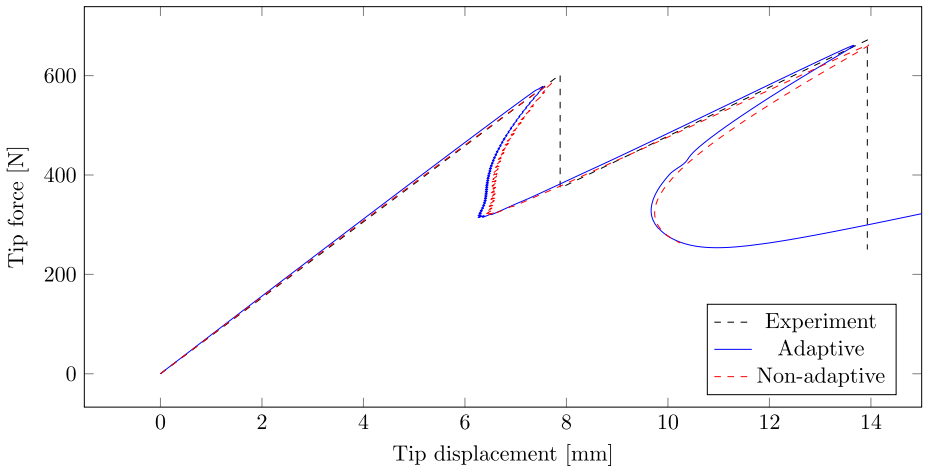

Fig. 9. Comparison between force–displacement response for the adaptive model, non-adaptive model, and experiment.

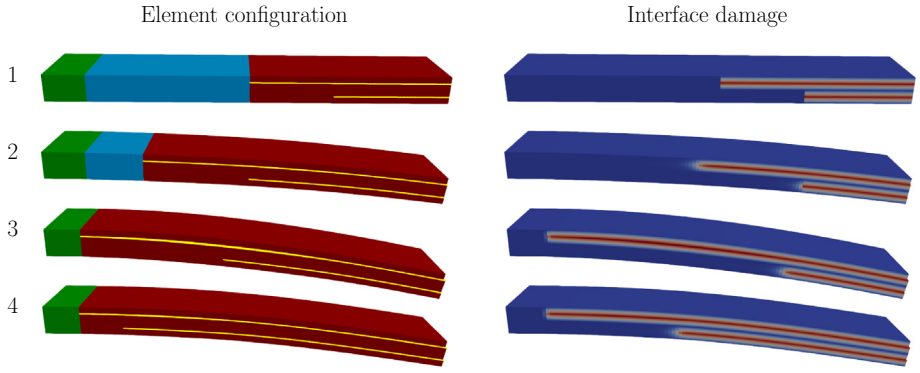

Fig. 10. The deformed cantilever beam at specific times of the simulations. Left: Element configuration (blue is *lumped*, green is *layered*, and red is *discontinuous*). Right: Interface damage parameter.

quent time steps, the elements are enhanced in order to allow for crack propagation in the top interface. The elements are however not enhanced for the lower crack, since no crack propagation is expected here. When the upper crack has reached the fixed end (time instant no 3), the loading on the second interface increases until the lower crack starts to propagate, whereby the elements are additionally refined with a second displacement discontinuity.

When comparing the efficiency gain between the adaptive and non-adaptive model, a speed up of 1.4 times is obtained until the first load drop. If we instead compare computational times all the way to the second load drop, the speed up is somewhat lower (1.3 times). The rather small efficiency gain comes from the fact that the initial cracks span a large part of the beam, meaning that the adaptive and non-adaptive models have relatively similar number of degrees of freedom. Furthermore, since the adaptive model is enhanced early in the simulation (due to the upper crack reaching the constrained boundary), the efficiency gain is even lower. Note that better efficiency gains would be obtained if the area with formed cracks are small compared to the rest of structure, or if a larger number of layers would be included in the model.

7. Conclusions and future work

In this paper, we demonstrate that the smoothness of the Isogeometric discretisation enables an efficient recovery of transverse stress components on element level, even for doubly curved shells. It is shown that this applies also to cases that are not restricted by cylindrical bending deformation, as is the case e.g. for the so-called extended 2D method [5,37,38]. The element-wise stress recovery method thereby allows for improved prediction of transverse stresses, which in turn can be used to predict where new delamination might initiate.

The adaptive isogeometric continuum element presented in this work takes advantage of the knot insertion technique from IGA. Thereby, it allows for simple and flexible enhancement of the kinematics in the areas of the model where delaminations initiate and propagate. The proposed shell enables a straightforward adaptation of the through-thickness discretisation, from an effective (or *lumped*) state that is able to accurately predict stiffness and in-plane stresses, into layer-wise and/or fully delaminated states that allows for accurate modelling of intra- and/or interlaminar failure. The capabilities of the adaptive shell element are demonstrated for the case of a doubly notched multilayered composite specimen loaded in bending. The numerical results show that the adaptive element with its extended kinematics is suitable for replicating a case of competing growth of two delamination cracks. A strong correlation is seen between the simulated force–displacement response and the experimentally obtained force–displacement response reported by Yasaee et al. [33]. It is also shown that the adaptive approach is accurately reproducing the results obtained from a shell model with pre-defined cohesive interfaces.

Declaration of Competing Interest

The authors declare that they have no known competing financial interests or personal relationships that could have appeared to influence the work reported in this paper.

Acknowledgements

The work in this paper has been funded by the Swedish Research Council through Grant No. 2018–05345. Financial support has in part also been provided by the Swedish Innovation Programme LIGHTer.

References

[1] Carrera E. Historical review of Zig-Zag theories for multilayered plates and shells. Appl Mech Rev 2003;56(3):287–308. https://doi.org/10.1115/1.1557614.
[2] Reddy JN. Mechanics of laminated composite plates and shells: theory and analysis. 2nd Ed. CRC Press; 2003.
[3] Carrera E, Cinefra M, Petrolo M, Zappino E. Finite Element Analysis of Structures through Unified Formulation. 1st Ed. Wiley; 2014.
[4] Grauers L, Olsson R, Gutkin R. Energy absorption and damage mechanisms in progressive crushing of corrugated NCF laminates: Fractographic analysis. Compos Struct 2014;110:110–7. https://doi.org/10.1016/j.compstruct.2013.11.001.
[5] Rolfes R, Rohwer K. Improved transverse shear stresses in composite finite elements based on first order shear deformation theory. Int J Numer Meth Eng 1997;40(1):51–60. https://doi.org/10.1002/(SICI)1097-0207(19970115)40:1<51::AID-NME49>3.0.CO;2-3.
[6] Daniel PM, Främby J, Fagerström M, Maimí P. Complete transverse stress recovery model for linear shell elements in arbitrarily curved laminates. Compos Struct 2020;252:112675. https://doi.org/10.1016/j.compstruct.2020.112675.
[7] Pinho ST, Iannucci L, Robinson P. Physically based failure models and criteria for laminated fibre-reinforced composites with emphasis on fibre kinking. Part II: FE implementation. Compos Part A: Appl Sci Manuf 2006;37(5):766–77. https://doi.org/10.1016/j.compositesa.2005.06.008.
[8] Maimí P, Camanho PP, Mayugo JA, Dávila CG. A continuum damage model for composite laminates: Part II – Computational implementation and validation. Mech Mater 2007;39(10):909–19. https://doi.org/10.1016/j.mechmat.2007.03.006.
[9] Louis N.S. Chiu, Brian G. Falzon, Bernard Chen, and Wenyi Yan. "Validation of a 3D damage model for predicting the response of composite structures under crushing loads". Composite Structures 147 (2016) 65–73. doi:10.1016/j.compstruct. 2016.03.028.
[10] Costa S, Bru T, Olsson R, Portugal A. Improvement and validation of a physically based model for the shear and transverse crushing of orthotropic composites. J Compos Mater 2019;53(12):1681–96. https://doi.org/10.1177/0021998318807964.
[11] Su ZC, Tay TE, Ridha M, Chen BY. Progressive damage modeling of open-hole composite laminates under compression. Compos Struct 2015;122:507–17. https://doi.org/10.1016/j.compstruct.2014.12.022.
[12] Thorsson SI, Waas AM, Rassaian M. Low-velocity impact predictions of composite laminates using a continuum shell based modeling approach part A: Impact study. Int J Solids Struct 2018;155:185–200. https://doi.org/10.1016/j.ijsolstr.2018.07.020.
[13] Shor OO, Vaziri R. Application of the local cohesive zone method to numerical simulation of composite structures under impact loading. Int J Impact Eng 2017;104:127–49. https://doi.org/10.1016/j.ijimpeng.2017.01.022.
[14] Selvaraj JL, Kawashita L, Allegri G, Hallett S. Adaptive Mesh Segmentation for Modelling Dynamic Delamination Initiation and Propagation in Thick Composite Laminates. In: 12th European LS-DYNA Conference, Koblenz.
[15] Pereira AB, de Morais AB. Mode I interlaminar fracture of carbon/epoxy multidirectional laminates. Compos Sci Technol 2004;64(13):2261–70. https://doi.org/10.1016/j.compscitech.2004.03.001.
[16] Heidari-Rarani M, Sayedain M. Finite element modeling strategies for 2D and 3D delamination propagation in composite DCB specimens using VCCT, CZM and XFEM approaches. Theoret Appl Fract Mech 2019;103:102246. https://doi.org/10.1016/j.tafmec.2019.102246.
[17] Brouzoulis J, Fagerström M. An enriched shell element formulation for efficient modeling of multiple delamination propagation in laminates. Compos Struct 2015;126:196–206. https://doi.org/10.1016/j.compstruct.2015.02.055.
[18] Remmers J.J.C., Wells G.N., and de Borst R. A solid-like shell element allowing for arbitrary delaminations. Int J Numer Meth Eng 2003; 58:2013–2040. doi:10.1002/nme. 907.
[19] Larsson R. A discontinuous shell-interface element for delamination analysis of laminated composite structures. Comput Methods Appl Mech Eng 2004;193(30):3173–94. https://doi.org/10.1016/j.cma.2003.08.009.
[20] McElroy M. Use of an enriched shell finite element to simulate delamination-migration in a composite laminate. Compos Struct 2017;167:88–95. https://doi.org/10.1016/j.compstruct.2017.01.057.
[21] Främby J, Fagerström M, Brouzoulis J. Adaptive modelling of delamination initiation and propagation using an equivalent single-layer shell approach. Int J Numer Meth Eng 2017;112(8):882–908. https://doi.org/10.1002/nme.5536.
[22] Adams C, Fagerström M, Remmers JJC. Efficient modelling of delamination growth using adaptive isogeometric continuum shell elements. Computational Mechanics 2020;65(1):99–117. https://doi.org/10.1007/s00466-019-01754-8.
[23] Kiendl J, Bletzinger K-U, Linhard J, Wüchner R. Isogeometric shell analysis with Kirchhoff-Love elements. Comput Methods Appl Mech Eng 2009;198(49):3902–14. https://doi.org/10.1016/j.cma.2009.08.013.
[24] Saman H, Remmers JJC, Verhoosel CV, de Borst R. An isogeometric continuum shell element for non-linear analysis. Computer Methods in Applied Mechanics and Engineering 2014;271:1–22. https://doi.org/10.1016/j.cma.2013.11.023.
[25] Dufour JE, Antolin P, Sangalli G, Auricchio F, Reali A. A cost-effective isogeometric approach for composite plates based on a stress recovery procedure. Composites Part B: Engineering 2018;138:12–8. https://doi.org/10.1016/j.compositesb.2017.11.026.
[26] Pressley A. Elementary Differential Geometry. 1st Ed. Springer; 2010.
[27] Piegl L, Tiller W. The NURBS Book. 2nd Ed. Springer-Verlag; 1996.
[28] Ochoa OO, Engblom JJ. Analysis of progressive failure in composites. Compos Sci Technol 1987;28(2):87–102. https://doi.org/10.1016/0266-3538(87)90092-3.
[29] Turon A, Dávila CG, Camanho PP, Costa J. An engineering solution for mesh size effects in the simulation of delamination using cohesive zone models. Eng Fract Mech 2007;74(10):1665–82. https://doi.org/10.1016/j.engfracmech.2006.08.025.
[30] Borden MJ, Scott MA, Evans JA, Hughes TJR. Isogeometric finite element data structures based on Bezier extraction of NURBS. Int J Numer Meth Eng 2011;87(1–5):15–47. https://doi.org/10.1002/nme.2968.
[31] Patton A, Antolin P, Kiendl J, Reali A. Efficient equilibrium-based stress recovery for isogeometric laminated curved structures. Compos Struct 2021;272:113975. https://doi.org/10.1016/J.COMPSTRUCT.2021.113975.
[32] Malvern LE. Introduction to the Mechanics of a Continuous Medium. 1st Ed. Pearson College Div; 1969.
[33] Yasaee M, Mohamed G, Hallett SR. Interaction of Z-pins with Multiple Mode II Delaminations in Composite Laminates. Exp Mech 2016;56(8):1363–72. https://doi.org/10.1007/s11340-016-0175-9.
[34] O'Brien T.K and Krueger R. Analysis of Ninety Degree Flexure Tests for Characterization Composite Transverse Tensile Strength. October. 2001. doi: NASATM-2001-211227ARL-TR-2568.
[35] Kolluri M, Hoefnagels JPM, Van Dommelen JAW, Geers MGD. Irreversible mixed mode interface delamination using a combined damage-plasticity cohesive zone enabling unloading. Int J Fract 2014;185(1-2):77–95. https://doi.org/10.1007/s10704-013-9899-z.
[36] Verhoosel CV, Remmers JJC, Gutierrez MA. A dissipation-based arc-length method for robust simulation of brittle and ductile failure. Int J Numer Meth Eng 2009;11(9):1290–321. https://doi.org/10.1002/nme.2447.
[37] Rolfes R, Rohwer K, Ballerstaedt M. Efficient linear transverse normal stress analysis of layered composite plates. Comput Struct 1998;68(6):643–52. https://doi.org/10.1016/S0045-7949(98)00097-2.
[38] Rohwer K, Rolfes R. Calculating 3D stresses in layered composite plates and shells. Mech Compos Mater 1998;34(4):355–62. https://doi.org/10.1007/BF02257903.